Three-Dimensional Nanofabrication by Electron-Beam Lithography and Directed Self-Assembly

by

Hyung Wan Do

B.S. Electrical Engineering
B.S. Business Economics and Management
California Institute of Technology, 2012

Submitted to the Department of Electrical Engineering and Computer Science
in Partial Fulfillment of the Requirements for the Degree of

Master of Science in Electrical Engineering and Computer Science

at the

MASSACHUSETTS INSTITUTE OF TECHNOLOGY

September 2014

© 2014 Massachusetts Institute of Technology. All rights reserved.

Signature of Author: ____
Department of Electrical Engineering and Computer Science
August 12, 2014

Certified by: ____
Karl K. Berggren
Professor of Electrical Engineering
Thesis Supervisor

Accepted by: ____
Leslie A. Kolodziejski
Professor of Electrical Engineering
Chairman of the Committee on Graduate Students

Three-Dimensional Nanofabrication by Electron-Beam Lithography and Directed Self-Assembly

by

Hyung Wan Do

Submitted to the Department of Electrical Engineering and Computer Science
on August 12, 2014 in Partial Fulfillment of the
Requirements for the Degree of
Master of Science in Electrical Engineering and Computer Science

Abstract

In this thesis, we investigated three-dimensional (3D) nanofabrication using electron-beam lithography (EBL), block copolymer (BCP) self-assembly, and capillary force-induced self-assembly. We first developed new processes for fabricating 3D nanostructures using a hydrogen silsesquioxane (HSQ) and poly(methylmeth-acrylate) (PMMA) bilayer resist stack. We demonstrated self-aligned mushroom-shaped posts and freestanding supported structures. Next, we used the 3D nanostructures as topographical templates guiding the self-assembly of polystyrene-*b*-polydimethylsiloxane (PS-*b*-PDMS) block copolymer thin films. We observed parallel cylinders, mesh-shaped structures, and bar-shaped structures in PDMS. Finally, we studied capillary force-induced self-assembly of linear nanostructures using a spin drying process. We developed a computation schema based on the pairwise collapse of nanostructures. We achieved propagation of information and built a proof of concept logic gate.

Thesis Supervisor: Karl K. Berggren
Title: Professor of Electrical Engineering

Acknowledgements

First of all, I would like to thank my advisor Professor Karl K. Berggren for his active guidance throughout my research. I have learned a lot from his invaluable advice on research as well as communication and writing skills.

I would like to acknowledge James Daley and Mark Mondol for training me on equipment and maintaining them in a good condition.

Jae-Byum Chang has helped me since the beginning of my research. He has taught me many useful nanofabrication techniques. He has always provided me with helpful feedback and advice on research and general graduate school life.

I would also like to thank the QNN group members and the block copolymer team members for productive discussions. Especially, Dr. Hong Kyoon Choi has taught me all about block copolymer processing.

Finally, I am grateful to my parents for their love and support. They were always encouraging and supporting me with their love. I would have not been able to get to where I am now without them.

This work was supported by Taiwan Semiconductor Manufacturing Company and National Science Foundation under Award Number DMR-1234169.

Contents

1. Introduction 15

1.1 Electron-beam lithography 15

1.2 Block copolymer self-assembly 17

1.3 Capillary force-induced self-assembly 19

References 22

2. Three-dimensional nanofabrication using HSQ/PMMA bilayer Resists 25

2.1 Introduction 25

2.2 Experimental 27

2.2.1 Single-dot exposure process 28

2.2.2 Double-area exposure process 29

2.2.3 Metrology 30

2.3 Results 32

2.3.1 Single-dot exposure process 32

2.3.2 Double-area exposure process 34

2.4 Discussion 35

2.5 Conclusions 38

References 39

3. Templated self-assembly of three-dimensional nanostructures in block copolymer thin films 41

3.1 Introduction 41

3.2 Experimental 42

3.2.1 Template fabrication 43

3.2.2 Block copolymer self-assembly 43

3.2.3 Reactive-ion etching 44

3.2.4 Metrology 44

3.3 Results 46

3.3.1 Mushroom-shaped post template 46

3.3.2 Supported cross grid template 47

3.4 Discussion 48

3.5 Conclusions 50

References 51

4. Collapse computation by capillary force-induced self-assembly 53

4.1 Introduction 53

4.2 Experimental 55

4.2.1 Nanostructure fabrication 55

4.2.2 Spin drying process 55

4.2.3 Metrology 56

4.3 Results 56

4.3.1 Paired collapse of nanostructures 56

4.3.2 Propagation of information 57

4.3.3 Collapse computation 59

4.4 Discussion 62

4.5 Conclusions 64

References 65

5. Summary and future direction 67

List of figures

Figure 1-1 Examples of 3D nanostructures created using EBL. (a) Three-level structures fabricated by consecutive overlay exposures.[5] (b) Freestanding bridges fabricated by low- and high-electron energy exposures.[11] (c) Staircase profiles fabricated by grayscale lithography.[7] (d) Undercut structures fabricated using a bilayer resist stack.[9] 16

Figure 1-2 Schematic diagram showing different morphologies and phase diagrams of BCPs.[20] Redrawn form reference 20. (a) Various equilibrium bulk morphologies: spheres (S); cylinders (C); gyroids (G); and lamellae (L). (b) A theoretical phase diagram calculated from self-consistent field theory. CPS is closely packed spheres. (c) An experimental phase diagram of polyisoprene-*b*-polystyrene (PIP-*b*-PS) where f_A is the volume fraction of polyisoprene. PL is perforated lamellae. 18

Figure 1-3 Examples of 3D patterns created from capillary force-induced self-assembly. (a) Coiled epoxy pillars.[23] (b) Photoresist needles assembled into nanoflowers.[24] (c) Carbon nanotubes assembled into a helix.[25] (d) Assembled HSQ pillars.[26] (e) Twisted epoxy pillars.[27] (f) Collapsed HSQ arcs.[28] 20

Figure 2-1 SEM image of a 3D supported cross grid structure from sample III fabricated by using the methods described in this chapter (tilt angle of 55°). Freestanding top layer was patterned in HSQ and supporting bottom layer was patterned in PMMA. The two layers were exposed in a single electron-beam writing step without intermediate alignment of the pattern. 27

Figure 2-2 Schematic diagram showing process steps for single-dot exposure process and double-area exposure process. (a) HSQ/PMMA bilayer resist stack was prepared with HSQ on top of PMMA. Both resist layers were exposed from above with an electron beam. The HSQ was overdosed relative to the PMMA, resulting in a larger top

structure and overhang. The result was mushroom-shaped posts. (b) The same resist stack as in (a) but the exposure was done by using two immediately sequential doses. In the first lithography step, the bottom layer features were exposed using a high dose, while in the second lithography step, the top layer features were exposed at a dose that was too low to affect the initial bottom layer exposure. The result was free standing linear HSQ structures supported by PMMA posts. 31

Figure 2-3 SEM images of posts created from a dot exposure. (a) A dose of 400 fC/dot (~2.5×10^6 electrons/dot) resulted in 35-nm-diameter HSQ posts and 22-nm-diameter PMMA posts. (b) A dose of 1600 fC/dot (~1.0×10^7 electrons/dot) resulted in 70-nm-diameter HSQ posts and 32-nm-diameter PMMA posts. Larger diameter posts in HSQ showed that HSQ was more dose sensitive than PMMA. 31

Figure 2-4 SEM images of 3D nanostructures fabricated from the single-dot exposure process. All structures were from sample II. The diameter of HSQ disks and PMMA posts as well as the difference between the two diameters increased as the dose was increased. 33

Figure 2-5 SEM images of 3D nanostructures fabricated from the single-dot exposure process. All structures were from sample II. (a) Mushroom-shaped post structures. (b) Closely spaced linear arrays of posts resulted in connected top layer HSQ patterns supported by PMMA posts in the underlayer. (c) Same post structures as in (a) but where 5.65 times less exposure dose was used. The structures collapsed during the development and drying process. 34

Figure 2-6 SEM images of 3D nanostructures fabricated from the double-area exposure process. The first structure was from sample III and the other two structures were from sample I. (a) Mushroom-shaped posts with well-defined top disks over lower posts (tilt angle of 55°). (b) Freestanding linear top layer structures with a lower layer post support (tilt angle of 45°). (c) Freestanding cross grid structures with a lower layer post support. 35

Figure 3-1 Schematic diagram showing process steps. HSQ/PMMA bilayer resist stack was prepared with HSQ on top of PMMA. 3D templates were fabricated using the double-area exposure process. The templates were chemically functionalized with a PDMS brush or PS brush. BCP film was spin coated and solvent annealed in a 5:1 mixture of toluene and heptane. The annealed BCP film was

reactive-ion etched to remove the top PDMS surface and the PS matrix. 45

Figure 3-2 SEM images of PDMS cylinders in the solvent annealed BCP film after RIE. Bright gray lines are the oxidized PDMS cylinders. (a) Monolayer BCP film. (b) Bilayer BCP film. Top and bottom layers were aligned in the same direction. 45

Figure 3-3 SEM images of PDMS patterns formed on mushroom-shaped post template. (a) PDMS-functionalized template. The PDMS cylinders were aligned parallel to each other with long range order. (b) PS-functionalized template. The PDMS cylinders formed mesh-shaped structures with poor long range order. 47

Figure 3-4 SEM images of PDMS patterns formed on supported cross grid template. Both templates were chemically functionalized with a PS brush. (a) The PDMS cylinders were formed over the top HSQ template when height of the bottom PMMA template was less than 40 nm. (b) No PDMS patterns were formed over the top HSQ template when height of the bottom PMMA template was greater than 60 nm. 48

Figure 4-1 Paired collapse of line structures. (a) Schematic diagram showing the paired collapse. Asymmetric menisci caused the line structures to collapse toward each other. (b) SEM image of the line structures with two different pitches. The structures were collapsed in pairs after spin drying. 57

Figure 4-2 Propagation of information. (a) Schematic diagram showing the propagation of information. Asymmetric capillary force was created in symmetric geometry by controlling the direction of the meniscus movement. (b) SEM image of parallel line structures collapsed in pairs after spin drying. A defect (circled in red) was caused by three line structures collapsed together. (c) SEM image of line structures rotated by 45° collapsed in pairs after spin drying. A defect (circled in red) was caused by an unpaired line structure. 59

Figure 4-3 Schematic diagram showing OR gate design. OR gate is indicated by a red hexagon. Line structures before (left) and after (right) spin drying are shown. The arrows indicate the pairing of the collapsed line structures as the meniscus moves from top to bottom. (a) Both inputs had two line structures (0 bit). The output had no unpaired line structures after collapse (0 bit). (b) Input A had one line

structure (1 bit) while input B had two line structures (0 bit). The output had one unpaired line structure after collapse (1 bit). (c) Both inputs had one line structure (1 bit). The output had one unpaired line structure after collapse (1 bit). Therefore, this is an OR gate. 61

Figure 4-4 SEM images of collapsed line structures in an OR gate. (a) Both inputs had four line structures (0 bit). The output had no unpaired line structures after collapse (0 bit). (b) The left input had three line structures (1 bit) while the right input had four line structures (0 bit). The output had one unpaired line structure after collapse (1 bit). (c) Both inputs had three line structures (1 bit). The output had three unpaired line structures after collapse (1 bit). The first two standing line structures should have been paired with each other. The third standing line structure should have been paired with the next line structure so that the unpaired line structure appears at the end of the output instead of the middle. 62

Chapter 1

Introduction

In this thesis, we explore three different methods of fabricating three-dimensional (3D) nanostructures: (1) electron-beam lithography (EBL); (2) block copolymer (BCP) self-assembly; and (3) capillary force-induced self-assembly. We provide a brief introduction to each of the three methods in this chapter.

1.1 Electron-beam lithography

Electron-beam lithography (EBL) has been used for several decades to overcome the diffraction-limited resolution of optical lithography. In EBL, patterns are exposed in the resist from above by a focused beam of electrons. Sub-10-nm structures have been demonstrated in both organic and inorganic resists.[1-4] Several approaches have been aimed at fabricating three-dimensional (3D) nanostructures using EBL because most practical devices have 3D structures. However, it is generally difficult to create 3D nanostructures using a single electron-beam writing step because EBL is a two-dimensional (2D) process.

A common approach to creating 3D nanostructures using EBL involves repeating the 2D patterning step multiple times.[5-6] This process requires a precise alignment between each layer. Several methods have been suggested to circumvent this problem, such as using a low-contrast resist[7] or using a bilayer resist stack.[8,9,10] Figure 1-1 shows examples of the 3D nanostructures that have been fabricated using different methods. However, these methods had restrictions on the feature size or the type of structures that could be fabricated. Therefore, a new 3D nanofabrication process that is simple, fast, and low-cost is desired.

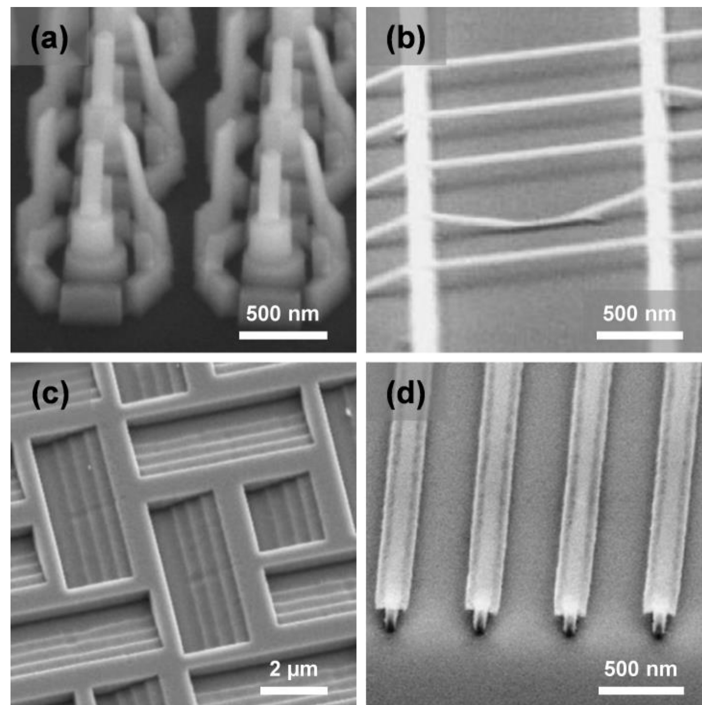

Figure 1-1: Examples of 3D nanostructures created using EBL. (a) Three-level structures fabricated by consecutive overlay exposures.[5] (b) Freestanding bridges fabricated by low- and high-electron energy exposures.[11] (c) Staircase profiles fabricated by grayscale lithography.[7] (d) Undercut structures fabricated using a bilayer resist stack.[9]

In Chapter 2, we describe two novel processes for fabricating self-aligned 3D nanostructures.

1.2 Block copolymer self-assembly

A block copolymer (BCP) is composed of two different polymer blocks that are covalently bonded together in the middle. BCPs can microphase separate into different morphologies governed by the segregation strength χN and volume fraction f, where χ is the Flory-Huggins interaction parameter describing the incompatibility between the two polymer blocks and N is the degree of polymerization. Depending on these parameters, bulk BCPs show diverse morphologies including spheres, cylinders, gyroids, and lamellae. Figure 1-2 shows the different morphologies and phase diagrams of typical BCPs. Due to their ability to form small periodic structures, BCPs have attracted a lot of attention in the semiconductor industry. Moreover, BCPs are capable of forming complex 3D nanostructures, making them a potential material for 3D devices. However, achieving patterns with long-range order has been a challenge.

To achieve long-range order, templates have been used to guide the self-assembly of BCPs. One method is to use a chemical template where certain regions are chemically patterned to be preferential to one block of the BCP.[12-15] Polystyrene-*b*-polymethylmethacrylate (PS-*b*-PMMA) is widely used with these templates. Another method is to use a topographical template which is chemically

functionalized to be preferential to one block of the BCP.[16-19] Polystyrene-*b*-polydimethylsiloxane (PS-*b*-PDMS) is a common choice for these templates. In this thesis, we focus on the templated self-assembly of PS-*b*-PDMS. PS-*b*-PDMS is advantageous for applications in lithography because the high χ value enables better ordering, and the silicon containing PDMS blocks provide high etch resistance.

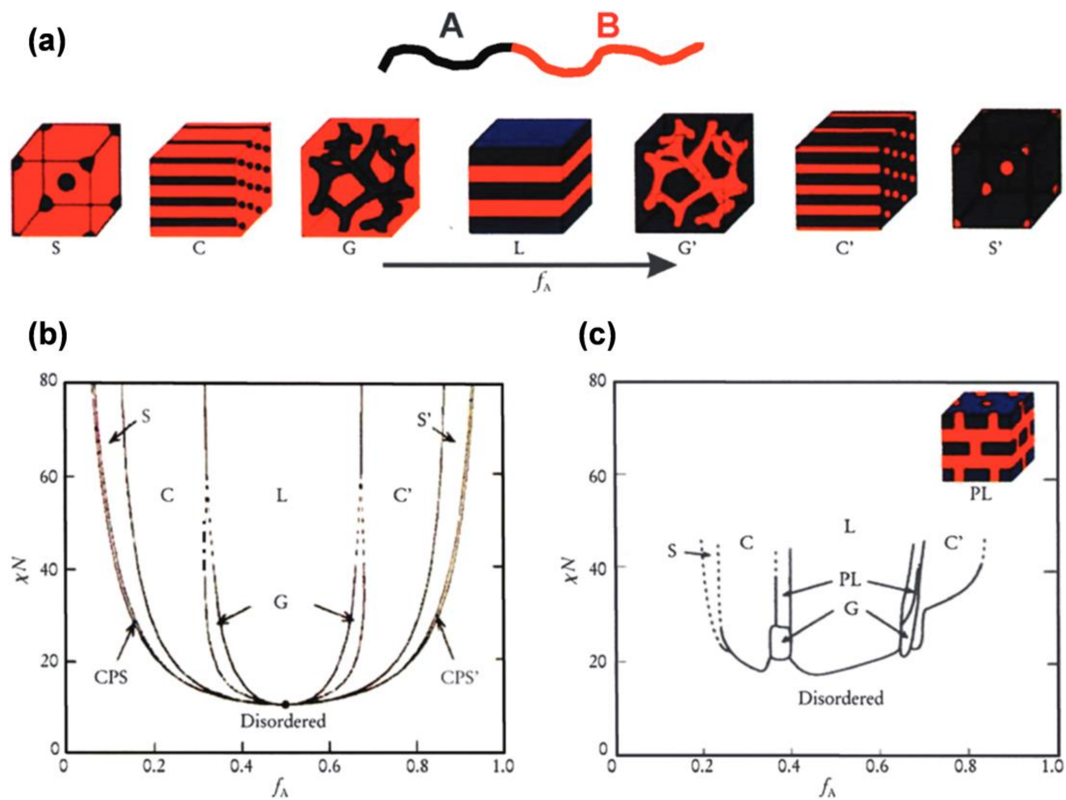

Figure 1-2: Schematic diagram showing different morphologies and phase diagrams of BCPs.[20] Redrawn form reference 20. (a) Various equilibrium bulk morphologies: spheres (S); cylinders (C); gyroids (G); and lamellae (L). (b) A theoretical phase diagram calculated from self-consistent field theory. CPS is closely packed spheres. (c) An experimental phase diagram of polyisoprene-*b*-polystyrene (PIP-*b*-PS) where f_A is the volume fraction of polyisoprene. PL is perforated lamellae.

In Chapter 3, we show 3D nanostructures in PS-*b*-PDMS BCP thin films where chemically functionalized 3D templates were used to direct the self-assembly process.

1.3 Capillary force-induced self-assembly

Capillary force plays a critical role in the fabrication of micro and nanostructures. During the resist development and the subsequent evaporation drying process, a liquid meniscus forms around the patterned structures. Therefore, a large capillary force is applied at the interface between liquid and air around the structures. When this force is larger than a critical force determined by the material properties and geometry of the structure, the structures are bent and eventually collapsed. Structure collapse is undesired in most cases, and many works have been done to prevent pattern collapse.[21,22]

Several attempts have been made to use the capillary force to drive the self-assembly of micro and nanostructures into complex hierarchical structures.[23-28] Such structures are useful because they have potential applications in device fabrication and high-throughput patterning. However, it is difficult to create arbitrary patterns using capillary force-induced self-assembly because the collapsing direction of structures is usually unpredictable. Duan et al. have recently shown control over the collapsing direction by varying the density of the nanopillars[26] and by creating linear nanostructures with asymmetric geometry.[28]

Figure 1-3 shows examples of the complex 3D patterns that have been self-assembled by capillary force-induced collapse. In these examples, however, the collapsing order of the nanostructures was not controlled. A new nanoscale pattern generation technique could be developed by engineering the self-assembly of nanostructure collapse.

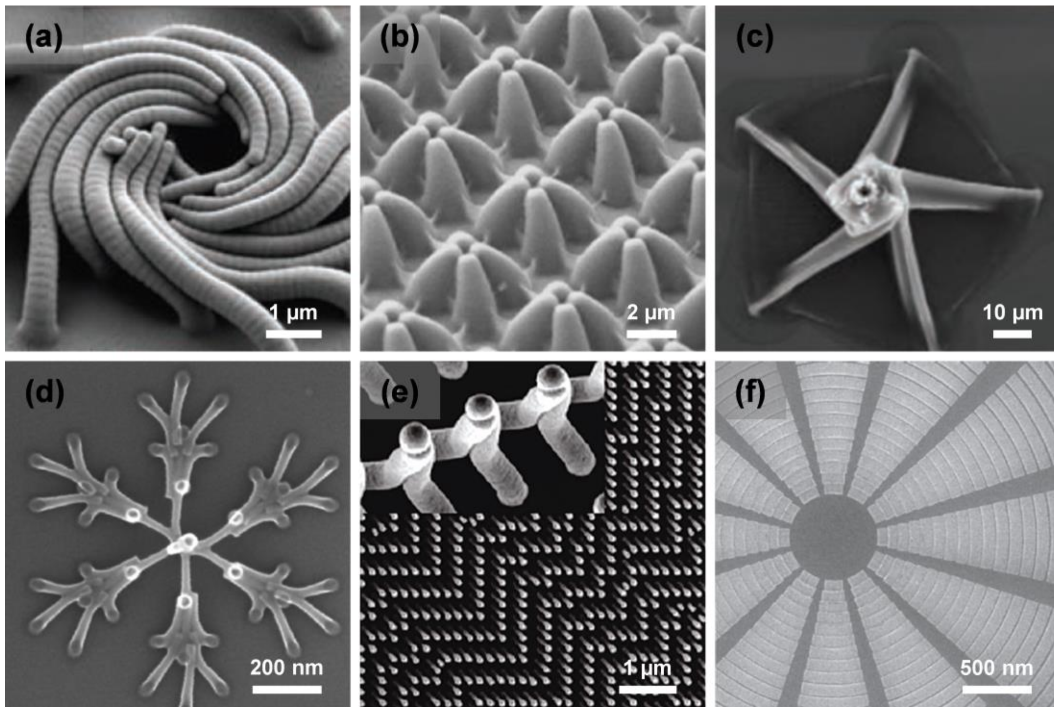

Figure 1-3: Examples of 3D patterns created from capillary force-induced self-assembly. (a) Coiled epoxy pillars.[23] (b) Photoresist needles assembled into nanoflowers.[24] (c) Carbon nanotubes assembled into a helix.[25] (d) Assembled HSQ pillars.[26] (e) Twisted epoxy pillars.[27] (f) Collapsed HSQ arcs.[28]

In Chapter 4, we demonstrate a method of controlling the collapsing order of the nanostructures as well as the collapsing direction. We show a computation

schema using capillary force-induced self-assembly that enables high-throughput patter generation.

References

1. J. K. W. Yang and K. K. Berggren, J. Vac. Sci. Technol. B **25,** 2025 (2007).
2. B. M. Cord, J. K. W. Yang, H. Duan, D. C. Joy, J. Klingfus, and K. K. Berggren, J. Vac. Sci. Technol. B **27,** 2616 (2009).
3. J. K. W. Yang, B. M. Cord, H. Duan, J. Klingfus, S.-W. Nam, K.-B. Kim, M. J. Rooks, and K. K. Berggren, J. Vac. Sci. Technol. B **27,** 2622 (2009).
4. H. Duan, D. Winston, J. K. W. Yang, B. M. Cord, V. R. Manfrinato, and K. K. Berggren, J. Vac. Sci. Technol. B **28,** C6C58 (2010).
5. J. Vila-Comamala, S. Gorelick, V. A. Guzenko, and C. David, J. Vac. Sci. Technol. B **29**, 06F301 (2011).
6. L. T. Varghese, L. Fan, J. Wang, Y. Xuan, and M. Qi, Small **9,** 4237 (2013).
7. A. Schleunitz and H. Schift, J. Micromech. Microeng. **20,** 095002 (2010).
8. B. M. Cord, C. Dames, J. Aumentado, and K. K. Berggren, J. Vac. Sci. Technol. B **24,** 3139 (2006).
9. H. Yang, A. Jin, Q. Luo, J. Li, C. Gu, and Z. Cui, Microelectron. Eng. **85,** 814 (2008).
10. H. Duan, H. Hu, H. K. Hui, Z. Shen, and J. K. W. Yang, Nanotechnology **24,** 185301 (2013).
11. Y. Matsubara, J. Taniguchi, and I. Miyamoto, Jpn. J. Appl. Phys. **45,** 5538 (2006).
12. S. O. Kim, H. H. Solak, M. P. Stoykovich, N. J. Ferrier, J. J. de Pablo, and P. F. Nealey, Nature **424,** 411 (2003).
13. M. P. Stoykovich, M. Muller, S. O. Kim, H. H. Solak, E. W. Edwards, J. J. de Pablo, and P. F. Nealey, Science **308,** 1142 (2005).
14. J. Y. Cheng, C. T. Rettner, D. P. Sanders, H.-C. Kim, and W. D. Hinsberg, Adv. Mater. **20,** 3155 (2008).
15. R. Ruiz, H. Kang, F. A. Detcheverry, E. Dobisz, D. S. Kercher, T. R. Albrecht, J. J. de Pablo, and P. F. Nealey, Science **321,** 936 (2008).
16. R. A. Segalman, H. Yokoyama, and E. J. Kramer, Adv. Mater. **13**, 1152 (2001).
17. J. Y. Cheng, C. A. Ross, E. L. Thomas, H. I. Smith, and G. J. Vancso, Appl. Phys. Lett. **81,** 3657 (2002).
18. I. Bita, J. K. W. Yang, Y. S. Jung, C. A. Ross, E. L. Thomas, and K. K. Berggren, Science **321,** 939 (2008).
19. S. Park, D. H. Lee, J. Xu, B. Kim, S. W. Hong, U. Jeong, T. Xu, and T. P. Russell, Science **323,** 1030 (2009).
20. F. S. Bates and G. H. Fredrickson, Phys. Today **52,** 32 (1999).
21. T. Tanaka, M. Morigami, and N. Atoda, Jpn. J. Appl. Phys., Part 1 **32,** 6059 (1993).
22. D. L. Goldfarb, J. J. de Pablo, P. F. Nealey, J. P. Simons, W. M. Moreau, and M. Angelopoulos, J. Vac. Sci. Technol. B **18,** 3313 (2000).

23. B. Pokroy, S. H. Kang, L. Mahadevan, and J. Aizenberg, Science **323,** 237 (2009).
24. D. Wu, Q.-D. Chen, B.-B. Xu, J. Jiao, Y. Xu, H. Xia, and H.-B. Sun, Appl. Phys. Lett. **95,** 091902 (2009).
25. M. De Volder, S. H. Tawfick, S. J. Park, D. Copic, Z. Zhao, W. Lu, and A. J. Hart, Adv. Mater. **22,** 4384 (2010).
26. H. Duan and K. K. Berggren, Nano Lett. **10,** 3710 (2010).
27. S. H. Kang, B. Pokroy, L. Mahadevan, and J. Aizenberg, Nano Lett. **4,** 6323 (2010).
28. H. Duan, J. K. W. Yang, and K. K. Berggren, Small **7,** 2661 (2011).

Chapter 2

Three-dimensional nanofabrication using HSQ/PMMA bilayer resists

In this work, we developed two processes for fabricating three-dimensional (3D) nanostructures using a hydrogen silsesquioxane (HSQ) and poly(methylmeth-acrylate) (PMMA) bilayer resist stack. The resist stack was patterned in a single electron-beam writing step without removing the wafer. The resulting 3D nanostructures naturally achieved vertical self-alignment without the need for any intermediate alignment. Self-aligned mushroom-shaped posts and freestanding supported structures were demonstrated.

2.1 Introduction

Three-dimensional (3D) devices are difficult to fabricate, but offer unique advantages over planar devices for many applications. There has been a growing interest in 3D devices such as photonic crystals and metamaterials,[1,2] and nanoelectromechanical systems (NEMS).[3] However, methods for generating 3D devices are generally slow and expensive. Therefore, a simple and rapid

fabrication process for complex 3D nanostructures is necessary. Methods for fabricating such 3D nanostructures using electron-beam lithography (EBL) include consecutive overlay exposures[4,5] or low- and high-electron energy exposures.[6,7,8] However, these approaches require alignment markers and accurate alignment routines for each additional layer. 3D nanostructures have also been fabricated using grayscale lithography,[9] but in this approach, the feature size was limited to several hundred nanometers.

A common approach used to circumvent the problem of 3D nanostructure fabrication is to use a bilayer resist stack.[10,11,12] Using a hydrogen silsesquioxane (HSQ) and poly(methylmethacrylate) (PMMA) bilayer resist stack, 3D nanostructures have been fabricated by patterning the top HSQ layer and reactive-ion etching of the bottom PMMA layer.[10,11] PMMA and poly(methylglutarimide) (PMGI) bilayer have also been used to pattern controlled 3D undercut structures.[12] However, these methods had restrictions on the final structures because all structures must be derived from only undercut structures.

Here, we describe self-aligned methods of fabricating 3D nanostructures using EBL of HSQ and PMMA, which allows more arbitrary patterns. HSQ is an inorganic, negative-tone, ultra-high resolution resist capable of resolving sub-10-nm half-pitch structures.[13,14] PMMA is an organic positive-tone resist that can also operate in negative-tone with ultra-high resolution when exposed to a dose

about 30 times higher than the positive dose.[15] In this work, we demonstrate two processes where the difference in dose sensitivity between HSQ and PMMA was used to produce self-aligned 3D nanostructures. Mushroom-shaped posts and freestanding supported structures were created without requiring feature alignment between layers. Figure 2-1 shows an example of a 3D nanostructure that was fabricated with our approach.

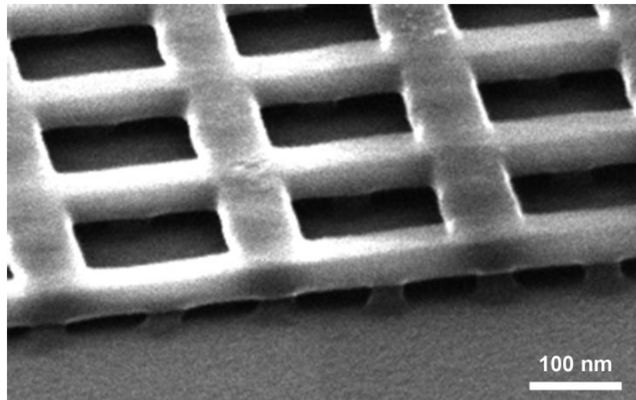

Figure 2-1: SEM image of a 3D supported cross grid structure from sample III fabricated by using the methods described in this chapter (tilt angle of 55°). Freestanding top layer was patterned in HSQ and supporting bottom layer was patterned in PMMA. The two layers were exposed in a single electron-beam writing step without intermediate alignment of the pattern.

2.2 Experimental

The key to realizing self-aligned 3D nanostructures on surfaces lies in designing an appropriate resist stack and electron-beam-exposure process. The process details were optimized to realize complex and well-supported 3D nanostructures with adequate dimensional control and precision. The resulting features were then

analyzed by using secondary electron imaging. We describe here two processes for 3D device fabrication, and the microscopy methods used to analyze the structures.

Figure 2-2 illustrates the fabrication steps required to create 3D nanostructures using HSQ/PMMA bilayer resists. We developed two processes: (1) figure 2-2(a) shows the single-dot exposure process; and (2) figure 2-2(b) shows the double-area exposure process. In both processes, we used the sensitivity difference between HSQ and PMMA to fabricate self-aligned 3D nanostructures. Figure 2-3 demonstrates the sensitivity difference between the two resists where a dot exposure using the same dose created structures with larger diameter in HSQ than in PMMA.

2.2.1 Single-dot exposure process

In the single-dot exposure process, we used a single exposure dose to pattern the bilayer resist stack. The resist stack was prepared by spin coating HSQ and PMMA on a silicon substrate. PMMA was spin coated first and was baked at 200°C for 2 min on a hot plate. HSQ was then spin coated on the PMMA. One sample was coated with 22 nm of PMMA followed by 22 nm of HSQ. A second sample was coated with 37 nm of PMMA followed by 28 nm of HSQ. A third sample was coated with 48 nm of PMMA followed by 39 nm of HSQ. We will refer to these as sample I, sample II, and sample III. The thickness was

determined by ellipsometry. A bilayer resist stack was formed without resist intermixing (step 1). A Raith 150 EBL system was used to expose dot arrays with doses ranging from 200 fC/dot (~1.2×10^6 electrons/dot) to 3200 fC/dot (~2.0×10^7 electrons/dot) at 30 kV acceleration voltage and 200 pA beam current. Because HSQ has higher dose sensitivity than negative-tone PMMA, the HSQ was overdosed relative to the PMMA. As a result, larger diameter HSQ disks were formed on top of smaller diameter PMMA posts (step 2). After exposure, the samples were developed in a high-contrast salty developer (1% NaOH and 4% NaCl in de-ionized water)[13] at 24°C for 4 min followed by a de-ionized water rinse for 3 min and blow drying with nitrogen (N_2) gas to remove unexposed HSQ. To remove lightly exposed PMMA and unexposed PMMA, the samples were sequentially developed in methyl isobutyl ketone (MIBK) at 18°C for 4 min,[15] spray rinsed with isopropanol (IPA) for 1 min, developed in acetone at 18°C for 3 min, and blown dry with N_2 gas (step 3).

2.2.2 Double-area exposure process

To better control the size and shape of the nanostructures on each resist layer, we developed a double-area exposure process in which smaller features on the bottom PMMA layer were defined using high dose exposures, and larger features on the top HSQ layer were defined using low dose exposures. Both layers were exposed in a single writing step without removing the wafer. In the double-area exposure process, the bilayer resist stack was prepared as in the single-dot

exposure process (step 1). A Raith 150 EBL system was used to expose arrays of 50-nm-diameter circles with a dose of 24000 μC/cm^2 (~1500 electrons/nm^2). During this step, 65-nm-diameter circular disks were formed in the HSQ layer due to overdose (step 2). In the same writing step, 75 nm × 2 μm rectangles were exposed over the circles with a dose of 4000 μC/cm^2 (~250 electrons/nm^2). This dose was sufficient to crosslink the HSQ, but was insufficient to severely affect the PMMA. Therefore, the rectangular line structures were only formed in the HSQ layer (step 3). After development, the lightly exposed PMMA under the HSQ line structures were removed and freestanding 3D nanostructures were formed (step 4).

2.2.3 Metrology

Metrology was performed by examining the 3D nanostructures using a scanning electron microscope (SEM). Top down SEM images were acquired using a Raith 150 scanning electron microscope operated with 10 kV acceleration voltage and 6 mm working distance. Tilted SEM images were obtained using a Zeiss Orion helium ion microscope and FEI Helios dual beam system. The operating conditions were 35 kV and 10 mm for the helium ion microscope, and 5 kV and 4 mm for the dual beam system.

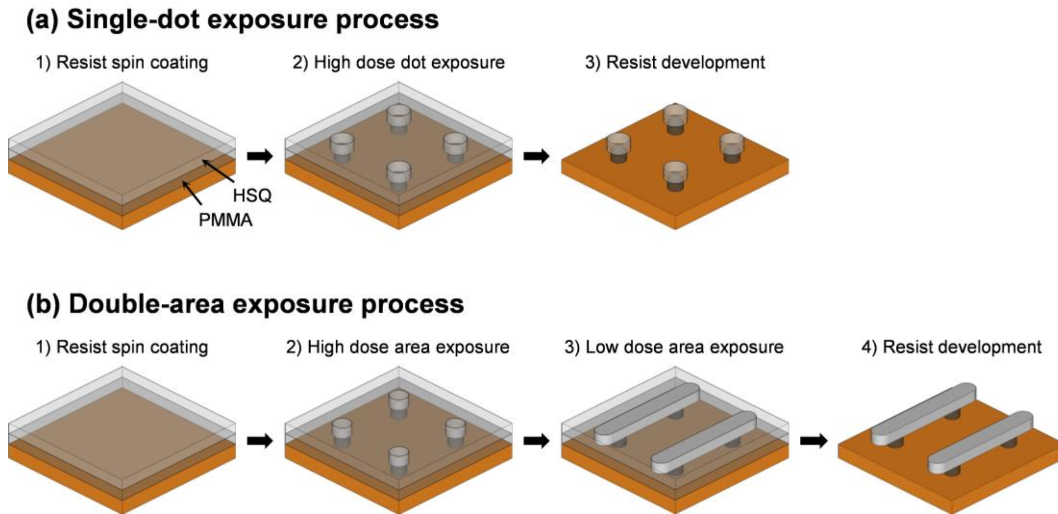

Figure 2-2: Schematic diagram showing process steps for single-dot exposure process and double-area exposure process. (a) HSQ/PMMA bilayer resist stack was prepared with HSQ on top of PMMA. Both resist layers were exposed from above with an electron beam. The HSQ was overdosed relative to the PMMA, resulting in a larger top structure and overhang. The result was mushroom-shaped posts. (b) The same resist stack as in (a) but the exposure was done by using two immediately sequential doses. In the first lithography step, the bottom layer features were exposed using a high dose, while in the second lithography step, the top layer features were exposed at a dose that was too low to affect the initial bottom layer exposure. The result was free standing linear HSQ structures supported by PMMA posts.

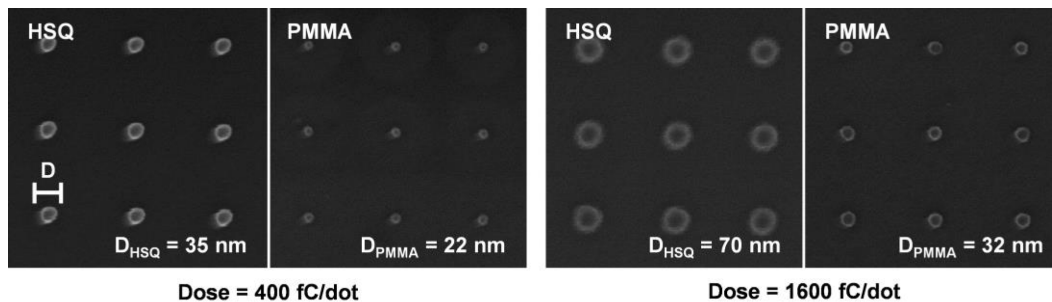

Figure 2-3: SEM images of posts created from a dot exposure. (a) A dose of 400 fC/dot (~2.5×10^6 electrons/dot) resulted in 35-nm-diameter HSQ posts and 22-nm-diameter PMMA posts. (b) A dose of 1600 fC/dot (~1.0×10^7 electrons/dot) resulted in 70-nm-diameter HSQ posts and 32-nm-diameter PMMA posts. Larger diameter posts in HSQ showed that HSQ was more dose sensitive than PMMA.

2.3 Results

By using the methods described in the previous section, we were able to fabricate a range of 3D nanostructures including mushroom-shaped posts, supported lines, and supported cross grids. Here, we describe those results so that we can draw conclusions about which methods are preferred under different circumstances.

2.3.1 Single-dot exposure process

Figures 2-4 and 2-5 show the 3D nanostructures fabricated using the single-dot exposure process, demonstrating overhung structures. In figure 2-4, 200 nm × 200 nm pitch dot arrays were exposed at a dose ranging from 200 fC/dot (~1.2×10^6 electrons/dot) to 3200 fC/dot (~2.0×10^7 electrons/dot). We observed an increase in diameter in both HSQ disks and PMMA posts as the dose was increased. In figure 2-5(a), the dot arrays were exposed at a dose of 3200 fC/dot (~2.0×10^7 electrons/dot), resulting in 108-nm-diameter HSQ disks and 40-nm-diameter PMMA posts. Such mushroom-shaped posts were created due to the sensitivity difference between the two resists. The diameter of both structures was determined by the single-dot exposure dose and the structures thus naturally achieved vertical self-alignment. In figure 2-5(b), 200 nm × 75 nm pitch dot arrays were exposed at a dose of 1132 fC/dot (~7.1×10^6 electrons/dot). Because the dots were positioned sufficiently close to each other, neighboring, 57-nm-diameter HSQ disks merged and formed wavy lines on top of 28-nm-diameter PMMA posts.

Pattern collapse was observed as shown in figure 2-5(c) when care was not taken during the development and drying process. Here, the HSQ layer was 28 nm thick and the PMMA layer was 37 nm thick. The dot arrays were exposed at a dose of 566 fC/dot (~3.5×10^6 electrons/dot), resulting in 40-nm-diameter HSQ disks and 24-nm-diameter PMMA posts. The collapsed nanostructures clearly showed the two resist materials as indicated in the inset of figure 2-5(c).

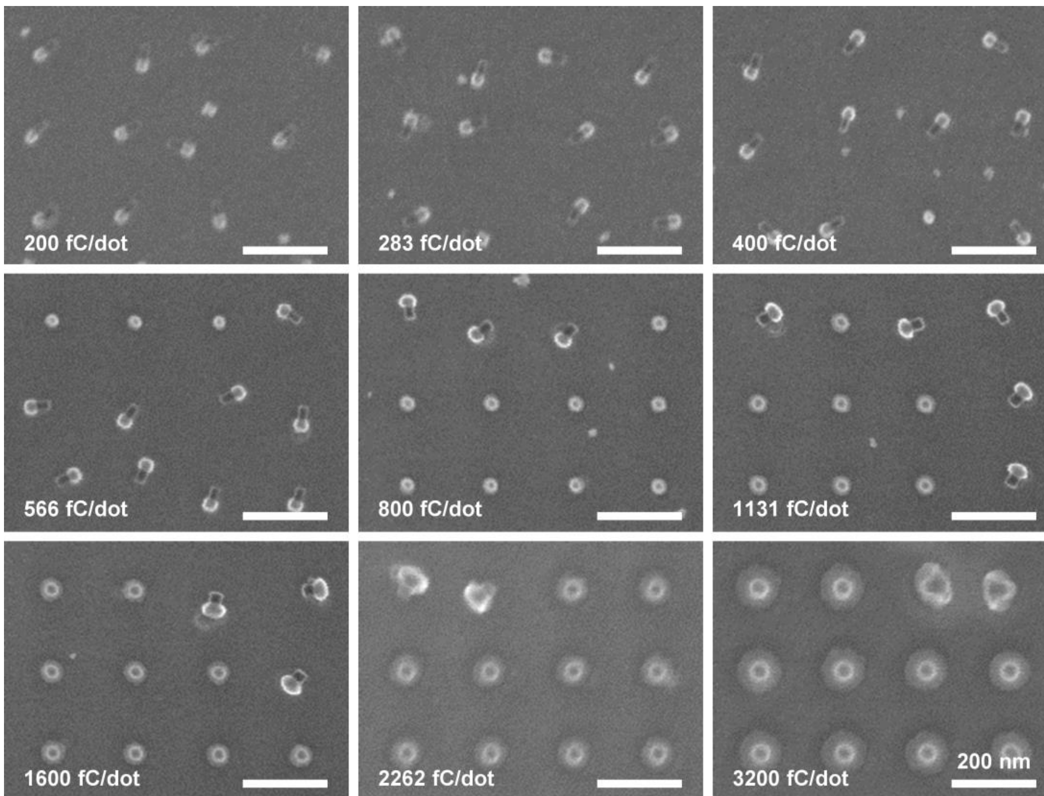

Figure 2-4: SEM images of 3D nanostructures fabricated from the single-dot exposure process. All structures were from sample II. The diameter of HSQ disks and PMMA posts as well as the difference between the two diameters increased as the dose was increased.

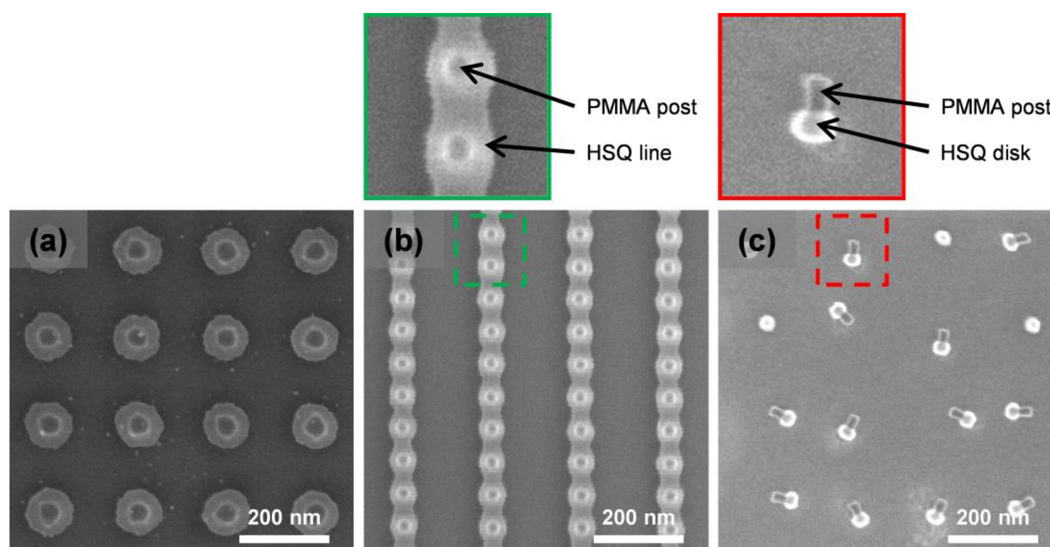

Figure 2-5: SEM images of 3D nanostructures fabricated from the single-dot exposure process. All structures were from sample II. (a) Mushroom-shaped post structures. (b) Closely spaced linear arrays of posts resulted in connected top layer HSQ patterns supported by PMMA posts in the underlayer. (c) Same post structures as in (a) but where 5.65 times less exposure dose was used. The structures collapsed during the development and drying process.

2.3.2 Double-area exposure process

The 3D nanostructures fabricated using the double-area exposure process are shown in figure 2-6. In figure 2-6(a), 75-nm-diameter disks were patterned in HSQ using low dose exposures, and 50-nm-diameter posts were patterned in PMMA using high dose exposures. Mushroom-shaped nanostructures similar to those in figures 2-4, 2-5(a), and 2-5(c) could be created with more dimensional precision than could be achieved in the single-dot exposure process. Figure 2-6(b) shows 60-nm-wide line structures in HSQ supported by 30-nm-diameter PMMA posts. The tilted SEM image demonstrated that the line structures were truly freestanding. Since features on each resist layer could be more accurately

controlled using the double-area exposure process, complex 3D nanostructures could be fabricated as shown in figure 2-6(c), where a 75-nm-wide cross grid was supported by 50-nm-diameter PMMA posts.

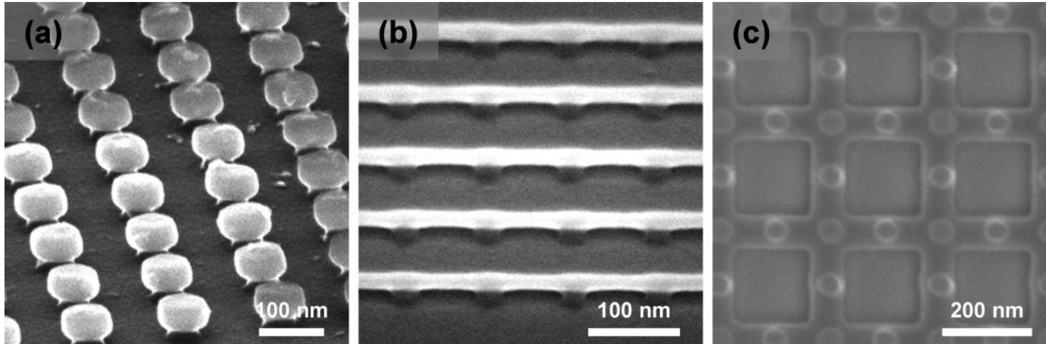

Figure 2-6: SEM images of 3D nanostructures fabricated from the double-area exposure process. The first structure was from sample III and the other two structures were from sample I. (a) Mushroom-shaped posts with well-defined top disks over lower posts (tilt angle of 55°). (b) Freestanding linear top layer structures with a lower layer post support (tilt angle of 45°). (c) Freestanding cross grid structures with a lower layer post support.

2.4 Discussion

A number of non-idealities were encountered and lessons learned as a result of our work. The single-dot exposure process could be thought of as a special case of the double-area exposure process where dot arrays are exposed in the high dose exposure step, and the low dose exposure step is omitted. Therefore, the single-dot exposure process proved more difficult to control than the double-area exposure process, from the perspective of both structure dimensions and edge roughness. Furthermore, overhung structures resulted in pattern collapse in the

single-dot exposure process. The causes and remedies for these observations are discussed here.

We were able to better control the size and shape of the nanostructures on each resist layer by using the double-area exposure process than using the single-dot exposure process. Mushroom-shaped posts shown in figures 2-4, 2-5(a), 2-5(c), and 2-6(a) could be fabricated using both processes. However, it was difficult to independently control the features on each resist layer in the single-dot exposure process because both layers were patterned by a single exposure dose. Therefore, the nanostructures in the top layer and the bottom layer had the same shape with only a difference in size. The possible structures were limited to mushroom-shaped posts (figures 2-4, 2-5(a), and 2-5(c)) and structures formed from merged posts (figure 2-5(b)). On the other hand, it was possible to precisely control the feature dimensions in the double-area exposure process as long as the size of the low dose exposure was larger than the size of the structures already defined by the high dose exposure, since two separate exposure steps were used to pattern each resist layer. Using two exposure steps gave more freedom in designing the 3D nanostructures. Contrary to figure 2-5(b), figure 2-6(b) did not show any waviness in the top layer because the line structures were formed by exposing rectangular patterns rather than by merging neighboring disks. Figure 2-6(c) demonstrates one possible nanostructure that can only be created with the double-area exposure process, a HSQ cross grid supported by PMMA posts.

In the single-dot exposure process, the top HSQ disks showed significant edge roughness as the dot dose was increased. Figures 2-5(a) and 2-5(c) illustrate the difference in the edge roughness where the exposure dose used in 2-5(a) was 5.65 times the exposure dose used in 2-5(c). Because the bilayer resist stack was exposed with a dot dose necessary to achieve negative-tone PMMA, the sensitive HSQ layer was significantly overdosed when a high dose was used to expose both layers. As a result, the areal-dose-density slope at the critical dose for HSQ exposure was significantly lower than it would be for an area dose (where most of the dose comes from the well-defined primary beam, rather than backscattering and beam skirts). This lower dose-density-slope resulted in less well-defined feature edges. This issue was solved by using the double-area exposure process where the size of the structures was controlled by the dimensions of the exposed pattern rather than the dose.

Finally, we developed a simple way to avoid collapse. We observed that pattern collapse occurred during the PMMA development and drying process. Originally in the process, the samples were sonicated in 18°C acetone for 3 min to remove unexposed PMMA. This process was modified by removing the sonication step. In addition, the final structure was rinsed with a low surface tension liquid, IPA prior to drying.[16]

2.5 Conclusions

The two processes described in this work are advantageous compared to previous approaches in that the resulting 3D nanostructures are self-aligned and thus avoid the need for any alignment routine. We successfully fabricated various 3D nanostructures such as freestanding cross grid supported by posts. Other types of structures could be benefited from our method. For example, sheets supported by lines or grids could be used as nanochannels for nanofluidic devices. Moreover, we believe that our method can be extended to a multilayer resist stack with different resist combinations as long as the resist layers have different dose sensitivity to electron beam and do not intermix with each other. We also point out that feature sizes might be tuned further by varying the development process from layer to layer. We expect that this simple method for creating self-aligned 3D nanostructures will have potential applications in plasmonic structures and nanomechanical devices.

References

1. G. von Freymann, A. Ledermann, M. Thiel, I. Staude, S. Essig, K. Busch, and M. Wegener, Adv. Funct. Mater. **20,** 1038 (2010).
2. C. M. Soukoulis and M. Wegener, Nat. Photonics **5,** 523 (2011).
3. H. G. Craighead, Science **290,** 1532 (2000).
4. J. Vila-Comamala, S. Gorelick, V. A. Guzenko, and C. David, J. Vac. Sci. Technol. B **29**, 06F301 (2011).
5. L. T. Varghese, L. Fan, J. Wang, Y. Xuan, and M. Qi, Small **9,** 4237 (2013).
6. D. M. Tanenbaum, A. Olkhovets, and L. Sekaric, J. Vac. Sci. Technol. B **19,** 2829 (2001).
7. E. J. Boyd and R. J. Blaikie, Microelectron. Eng. **83,** 767 (2006).
8. Y. Matsubara, J. Taniguchi, and I. Miyamoto, Jpn. J. Appl. Phys. **45,** 5538 (2006).
9. J. Kim, D. C. Joy, and S.-Y. Lee, Microelectron. Eng. **84,** 2859 (2007).
10. H. Yang, A. Jin, Q. Luo, J. Li, C. Gu, and Z. Cui, Microelectron. Eng. **85,** 814 (2008).
11. H. Duan, H. Hu, H. K. Hui, Z. Shen, and J. K. W. Yang, Nanotechnology **24,** 185301 (2013).
12. B. M. Cord, C. Dames, J. Aumentado, and K. K. Berggren, J. Vac. Sci. Technol. B **24,** 3139 (2006).
13. J. K. W. Yang and K. K. Berggren, J. Vac. Sci. Technol. B **25,** 2025 (2007).
14. J. K. W. Yang, B. M. Cord, H. Duan, J. Klingfus, S.-W. Nam, K.-B. Kim, M. J. Rooks, and K. K. Berggren, J. Vac. Sci. Technol. B **27,** 2622 (2009).
15. H. Duan, D. Winston, J. K. W. Yang, B. M. Cord, V. R. Manfrinato, and K. K. Berggren, J. Vac. Sci. Technol. B **28,** C6C58 (2010).
16. T. Tanaka, M. Morigami, and N. Atoda, Jpn. J. Appl. Phys., Part 1 **32,** 6059 (1993).

Chapter 3

Templated self-assembly of three-dimensional nanostructures in block copolymer thin films

In this work, we describe a method of templating three-dimensional (3D) nanostructures in polystyrene-*b*-polydimethylsiloxane (PS-*b*-PDMS) block copolymer thin films. Chemically functionalized 3D nanostructures were used as topographical templates guiding the self-assembly of the PS-*b*-PDMS block copolymer. Parallel cylinders, mesh-shaped structures, and bar-shaped structures in PDMS were observed.

3.1 Introduction

Block copolymers (BCPs) can microphase separate into complex nanostructures, forming periodic and well-ordered patterns over a large area. It has been shown that chemical[1-4] or topographical[5-8] templates can direct the self-assembly of BCP thin films. Chemically functionalized topographical templates using posts fabricated from electron-beam lithography (EBL) have been used to guide the

self-assembly of polystyrene-*b*-polydimethylsiloxane (PS-*b*-PDMS) BCP.[7,9-12] Functioning devices have been demonstrated using these patterns as lithography masks.[13-16]

BCP microdomains can form complex three-dimensional (3D) nanostructures, and therefore could be used to fabricate 3D devices.[17] Sequential stacking of two-dimensional (2D) BCP patterns has been used to create 3D patterns.[18,19,20] To avoid long process time and alignment between each layer, 3D patterns have also been created directly in a single step.[11,21,22] However, the final structures were limited to structures derived from hexagonally packed spheres and parallel cylinders.

In this chapter, we describe a new method of creating 3D BCP patterns by using chemically functionalized 3D templates. The templates were fabricated from a hydrogen silsesquioxane (HSQ) and poly(methylmethacrylate) (PMMA) bilayer resist stack using the double-area exposure process. We demonstrate 3D nanostructures in PS-*b*-PDMS BCP films using mushroom-shaped posts and freestanding supported cross grids as topographical templates.

3.2 Experimental

To achieve 3D nanostructures in BCP thin films, we used EBL to fabricate 3D templates and flow-controlled solvent annealing system to facilitate the self-

assembly process. Here, we describe the methods for generating 3D BCP patterns, and the metrology used to examine the 3D patterns. Figure 3-1 shows the major steps of the process.

3.2.1 Template fabrication

We used the double-area exposure process developed in the previous chapter to fabricate the 3D templates (steps 1 and 2). The double-area exposure process was chosen over the single-dot exposure process because we were able to better control the size and shape of the nanostructures on each resist layer. Mushroom-shaped posts and freestanding supported cross grids were fabricated and used as templates for the BCP self-assembly.

3.2.2 Block copolymer self-assembly

First, the templates were chemically functionalized with a hydroxyl-terminated PDMS brush (0.8 kg/mol) or PS brush (11 kg/mol) by spin coating 1% brush solution in propylene glycol monomethyl ether acetate (PGMEA) and annealing the samples in a vacuum oven at 170°C for 16 h (step 3). The samples were rinsed with toluene after annealing. Next, 2% PS-*b*-PDMS (45.4 kg/mol, f_{PDMS} = 33.5%) solution in PGMEA was spin coated onto the templated substrate and solvent annealed using a flow-controlled solvent annealing system (step 4). We used a 5:1 mixture of toluene and heptane where nitrogen (N_2) gas was bubbled through a chamber containing the solvent mixture at a flow rate of 10 sccm. The solvent

vapor was diluted with N_2 gas at a flow rate of 0.5 sccm. The annealing was done at room temperature for 3 h. The samples were quenched with N_2 gas after annealing. The equilibrium period of the PDMS cylinders was approximately 39 nm.

3.2.3 Reactive-ion etching

Reactive-ion etching (RIE) of the annealed BCP film was performed in two steps (step 5). First, CF_4 RIE was done for 5 s with a power of 50 W and pressure of 15 mTorr. This step removed the top PDMS surface. Next, O_2 RIE was done for 22 s with a power of 90 W and pressure of 6 mTorr. This step removed the PS matrix and oxidized the PDMS cylinders. Figure 3-2 shows the solvent annealed BCP film on a PS-functionalized untemplated substrate after RIE.

3.2.4 Metrology

We performed metrology by examining the 3D templates and the reactive-ion etched BCP films using a scanning electron microscope (SEM). Top down SEM images were obtained using a Raith 150 scanning electron microscope operated with 10 kV acceleration voltage and 6 mm working distance. Tilted SEM images were obtained using a FEI Helios dual beam system operated with 5 kV acceleration voltage and 4 mm working distance.

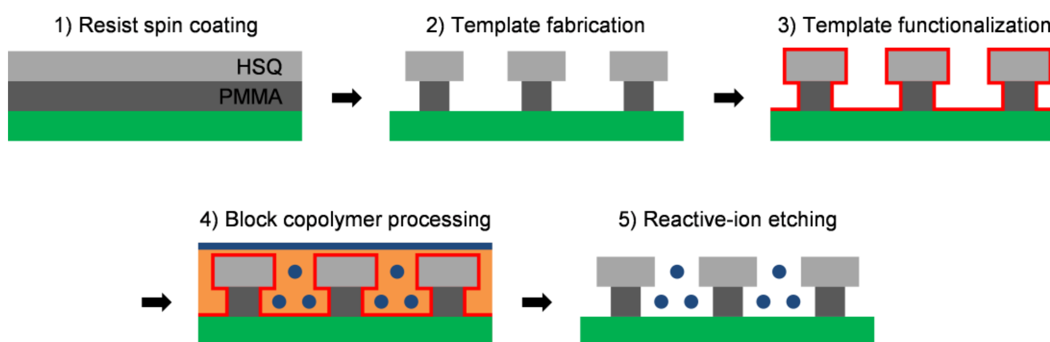

Figure 3-1: Schematic diagram showing process steps. HSQ/PMMA bilayer resist stack was prepared with HSQ on top of PMMA. 3D templates were fabricated using the double-area exposure process. The templates were chemically functionalized with a PDMS brush or PS brush. BCP film was spin coated and solvent annealed in a 5:1 mixture of toluene and heptane. The annealed BCP film was reactive-ion etched to remove the top PDMS surface and the PS matrix.

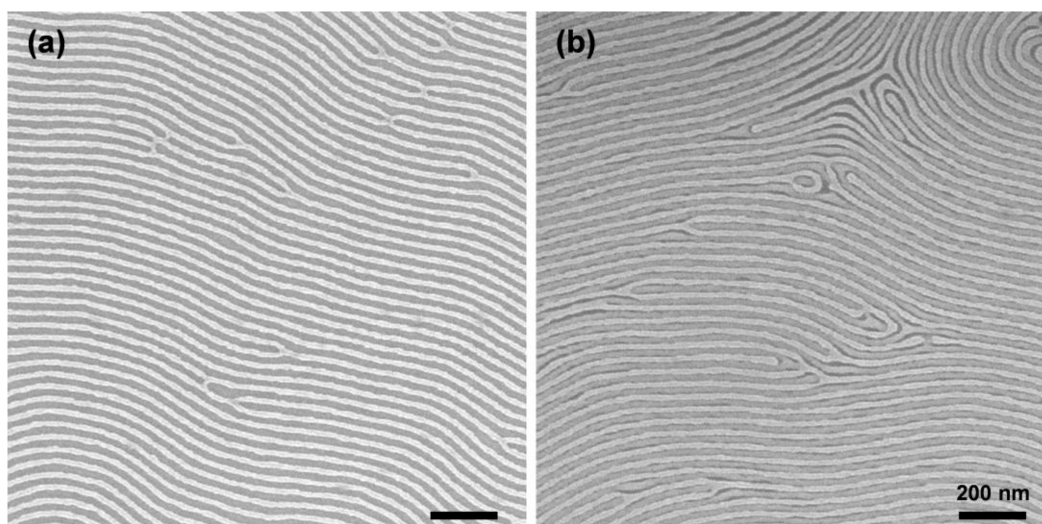

Figure 3-2: SEM images of PDMS cylinders in the solvent annealed BCP film after RIE. Bright gray lines are the oxidized PDMS cylinders. (a) Monolayer BCP film. (b) Bilayer BCP film. Top and bottom layers were aligned in the same direction.

3.3 Results

We were able to fabricate various 3D templates using the double-area exposure process. The templates we focused on were mushroom-shaped posts, cross grids supported by posts, and cross grids supported by lines. BCP film was annealed on these templates and reactive-ion etched for imaging. Here, we describe the resulting PDMS patterns.

3.3.1 Mushroom-shaped post template

For each sample, arrays of mushroom-shaped posts with pitches ranging from 120 nm to 185 nm were fabricated. Figure 3-3 shows the PDMS patterns that were formed on the mushroom-shaped post template. The diameter of the top HSQ disks was 60 nm and the diameter of the bottom PMMA posts was 30 nm. In figure 3-3(a), the template was chemically functionalized with a PDMS brush. Both HSQ and PMMA layers were 22 nm thick. The mushroom-shaped posts had a horizontal pitch of 125 nm and a vertical pitch of 83 nm. Both layers of the PDMS patterns were aligned in the same direction and had long-range order. The top PDMS patterns were formed on top of the template. In figure 3-3(b), the template was functionalized with a PS brush. The HSQ layer was 29 nm thick and the PMMA layer was 27 nm thick. The mushroom-shaped posts had a horizontal pitch of 152 nm and a vertical pitch of 101 nm. The top PDMS patterns formed mesh-shaped structures unlike the PDMS patterns from the PDMS-functionalized template. However, the PDMS patterns showed poor long-range order.

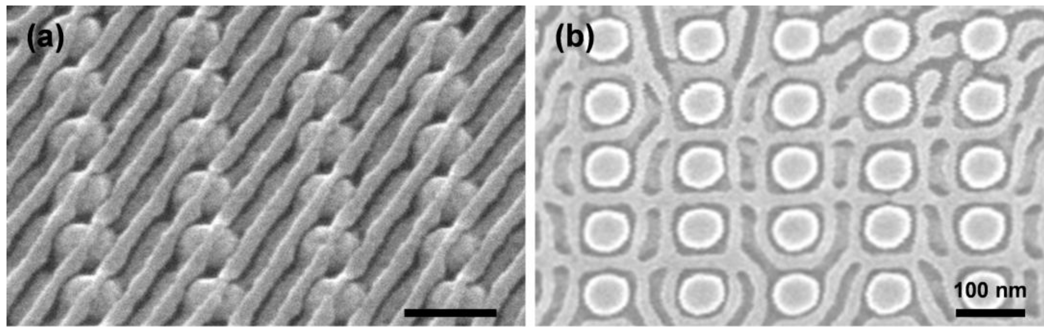

Figure 3-3: SEM images of PDMS patterns formed on mushroom-shaped post template. (a) PDMS-functionalized template. The PDMS cylinders were aligned parallel to each other with long-range order. (b) PS-functionalized template. The PDMS cylinders formed mesh-shaped structures with poor long-range order.

3.3.2 Supported cross grid template

For each sample, arrays of supported cross grids were fabricated with grid sizes ranging from 70 nm to 242 nm. PDMS patterns formed on the supported cross grid template are shown in figure 3-4. Both templates were functionalized with a PS brush. In figure 3-4(a), 50-nm-wide HSQ cross grid was supported by 30-nm-diameter PMMA posts. The HSQ layer was 29 nm thick and the PMMA layer was 27 nm thick. The size of the square in the cross grid was 142 nm. The PDMS patterns were formed on top of the cross grid. In figure 3-4(b), 50-nm-wide HSQ cross grid was supported by 30-nm-wide vertical PMMA lines. The HSQ layer was 29 nm thick and the PMMA layer was 63 nm thick. The size of the square in the cross grid was 214 nm. The PDMS patterns formed horizontally aligned or vertically aligned bar-shaped structures inside the cross grid. No PDMS patterns were found on top of the cross grid.

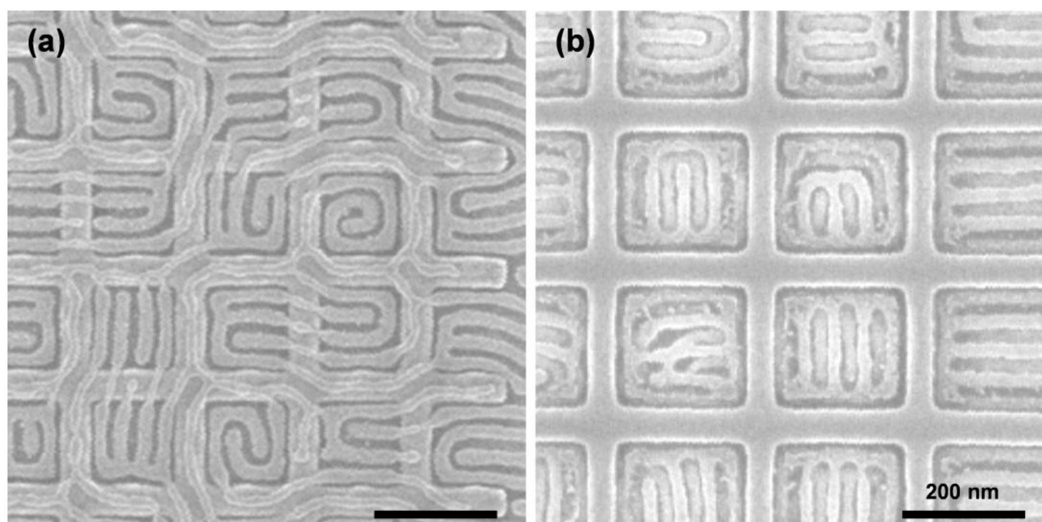

Figure 3-4: SEM images of PDMS patterns formed on supported cross grid template. Both templates were chemically functionalized with a PS brush. (a) The PDMS cylinders were formed over the top HSQ template when height of the bottom PMMA template was less than 40 nm. (b) No PDMS patterns were formed over the top HSQ template when height of the bottom PMMA template was greater than 60 nm.

3.4 Discussion

Minority block PDMS brush and majority block PS brush had different effects on the long-range order as well as the final structure of the PDMS patterns. In addition, different 3D template shapes resulted in different PDMS patterns. However, we were not able to form the PDMS patterns under the freestanding bridges. We discuss these observations here.

PDMS-functionalized templates showed a better long-range order than PS-functionalized templates, agreeing with previous observations.[23] Although the mushroom-shaped posts in figure 3-3(a) had a diameter much larger than the 10-

nm-diameter posts previously used to template PS-*b*-PDMS BCP with PDMS brush,[9] the mushroom-shaped posts still had an effect in ordering the PDMS patterns. The top PDMS patterns were formed on top of the template because the mushroom-shaped posts were too large to be incorporated into the PDMS cylinders. When PS brush was used in figure 3-3(b), the template no longer had to be incorporated into the PDMS cylinders and more complex patterns could be formed. The top PDMS cylinders formed mesh-shaped structures while the bottom PDMS cylinders formed parallel structures. The poor long-range order can be attributed to the effect of the majority block PS brush and the insufficient optimization in the parameters of the solvent annealing process. Moreover, the size and pitch of the templates were large compared to the equilibrium period of the BCP, which was undesirable for achieving long range order.

When supported cross grid templates were used, the PDMS cylinders were confined inside the cross grid. The PDMS cylinders were formed on top of the template when the PMMA height was less than 40 nm because the swollen BCP film thickness was greater than the template height. In figure 3-4(a), the confined PDMS patterns were connected to each other by the PDMS cylinders over the template. However, the PDMS cylinders did not form on top of the template when the PMMA height was greater than 60 nm. In figure 3-4(b), the confined PDMS patterns were therefore not connected to each other and bar-shaped structures were formed. This was comparable to the formation of concentric ring structures

when PS-*b*-PDMS was confined in circular trenches.[24] For both template heights, the PDMS patterns were not formed under the freestanding bridges. No connections between the confined PDMS patterns were observed under the bridges. Therefore, the PDMS patterns shown in figure 3-4 were controlled only by the top HSQ cross grid template, and the bottom PMMA posts or lines did not have any templating effect. We believe that as the BCP film swells during the solvent annealing process, the BCPs under the freestanding bridges swell outside of the bridges so that there are insufficient BCPs to form the PDMS patterns under the freestanding structures. We will investigate different annealing methods in the future to solve this issue.

3.5 Conclusions

The methods described in this chapter allow 3D nanostructures in BCP thin films to be formed where each layer is controlled by a different template shape. Self-aligned 3D nanostructures fabricated from the double-area exposure process allowed complex 3D templates to be used. Although incomplete, we showed that each BCP layer could have different morphologies controlled by the same 3D template. We believe that our process will work better with thermal annealing where the BCP film does not swell during the annealing process. Our method could potentially be used to fabricate 3D devices directly from BCP lithography.

References

1. S. O. Kim, H. H. Solak, M. P. Stoykovich, N. J. Ferrier, J. J. de Pablo, and P. F. Nealey, Nature **424,** 411 (2003).
2. M. P. Stoykovich, M. Muller, S. O. Kim, H. H. Solak, E. W. Edwards, J. J. de Pablo, and P. F. Nealey, Science **308,** 1142 (2005).
3. J. Y. Cheng, C. T. Rettner, D. P. Sanders, H.-C. Kim, and W. D. Hinsberg, Adv. Mater. **20,** 3155 (2008).
4. R. Ruiz, H. Kang, F. A. Detcheverry, E. Dobisz, D. S. Kercher, T. R. Albrecht, J. J. de Pablo, and P. F. Nealey, Science **321,** 936 (2008).
5. R. A. Segalman, H. Yokoyama, and E. J. Kramer, Adv. Mater. **13**, 1152 (2001).
6. J. Y. Cheng, C. A. Ross, E. L. Thomas, H. I. Smith, and G. J. Vancso, Appl. Phys. Lett. **81,** 3657 (2002).
7. I. Bita, J. K. W. Yang, Y. S. Jung, C. A. Ross, E. L. Thomas, and K. K. Berggren, Science **321,** 939 (2008).
8. S. Park, D. H. Lee, J. Xu, B. Kim, S. W. Hong, U. Jeong, T. Xu, and T. P. Russell, Science **323,** 1030 (2009).
9. J. K. W. Yang, Y. S. Jung, J.-B. Chang, R. A. Mickiewicz, A. Alexander-Katz, C. A. Ross, and K. K. Berggren, Nat. Nanotechnol. **5,** 256 (2010).
10. J.-B. Chang, J. G. Son, A. F. Hannon, A. Alexander-Katz, C. A. Ross, and K. K. Berggren, ACS Nano **6,** 2071 (2012).
11. A. Tavakkoli K. G., K. W. Gotrik, A. F. Hannon, A. Alexander-Katz, C. A. Ross, and K. K. Berggren, Science **336,** 1294 (2012).
12. J.-B. Chang, H. K. Choi, A. F. Hannon, A. Alexander-Katz, C. A. Ross, and K. K. Berggren, Nat. Commun. **5,** 3305 (2014).
13. T. Thurn-Albrecht, J. Schotter, G. A. Kastle, N. Emley, T. Shibauchi, L. Krusin-Elbaum, K. Guarini, C. T. Black, M. T. Tuominen, and T. P. Russell, Science **290,** 2126 (2000).
14. J. Y. Cheng, W. Jung, and C. A. Ross, Phys. Rev. B **70,** 064417 (2004).
15. C. T. Black, Appl. Phys. Lett. **87,** 163116 (2005).
16. Y. S. Jung, W. Jung, H. L. Tuller, and C. A. Ross, Nano Lett. **8,** 3776 (2008).
17. C. A. Ross, K. K. Berggren, J. Y. Cheng, Y. S. Jung, and J.-B. Chang, Adv. Mater. **26,** 4386 (2014).
18. F. Rose, J. K. Bosworth, E. A. Dobisz, and R. Ruiz, Nanotechnology **22,** 035603 (2011).
19. J. W. Jeong, W. I. Park, L.-M. Do, J.-H. Park, T.-H. Kim, G. Chae, and Y. S. Jung, Adv. Mater. **24,** 3526 (2012).
20. J. Y. Kim, B. H. Kim, J. O. Hwang, S.-J. Jeong, D. O. Shin, J. H. Mun, Y. J. Choi, H. M. Jin, and S. O. Kim, Adv. Mater. **25,** 1331 (2013).
21. Y. Wu, G. Cheng, K. Katsov, S. W. Sides, J. Wang, J. Tang, G. H. Fredrickson, M. Moskovits, and G. D. Stucky, Nat. Mater. **3,** 816 (2004).

22. V. P. Chuang, J. Y. Cheng, T. A. Savas, and C. A. Ross, Nano Lett. **6,** 2332 (2006).
23. Y. S. Jung and C. A. Ross, Nano Lett. **7,** 2046 (2007).
24. Y. S. Jung, W. Jung, and C. A. Ross, Nano Lett. **8,** 2975 (2008).

Chapter 4

Collapse computation by capillary force-induced self-assembly

In this work, we demonstrate capillary force-induced self-assembly of linear nanostructures into complex patterns. Collapsing order of the nanostructures was determined by a spin drying process where the direction of the meniscus movement was controlled. We showed pairwise collapse of nanostructures and used this phenomenon to develop a computation schema. We designed methods to achieve propagation of information and built a logic gate.

4.1 Introduction

Capillary force-induced collapse is a common phenomenon in nature. It is especially relevant to micro and nanostructure fabrication due to the evaporation drying process involved in the fabrication steps. Several works have been done on understanding the fundamentals of the process and preventing pattern collapse during the resist development.[1,2] Complex three-dimensional (3D) microstructures

have been self-assembled by capillary force using different materials such as polymers and carbon nanotubes.[3,4,5]

Collapse of high-aspect-ratio structures has also been demonstrated in nanoscale. Capillary force-induced self-assembly of nanopillars into ordered patterns has been shown at both 100 nm length scale[6] and 10 nm length scale.[7] Collapse of linear nanostructures has also been studied.[8,9] In particular, Duan et al. have combined nanocollapse self-assembly with electron-beam lithography (EBL) where asymmetric geometry was introduced to the linear nanostructures to control the collapse direction.[10] If we can control the collapsing order as well as the collapsing direction without introducing asymmetric geometry, we could develop a new nanoscale pattern generation technique capable of creating more complex 3D nanostructures.

Here, we describe a spin drying method of controlling the meniscus movement direction and therefore the collapsing order of the nanostructures. We combined this process with high resolution EBL of hydrogen silsesquioxane (HSQ)[11,12] to demonstrate pairwise collapse of nanostructures. We developed a computational schema by achieving propagation of information and showed a proof of concept logic gate.

4.2 Experimental

A key requirement for developing a computational schema based on capillary force-induced collapse of nanostructures is the ability to control the order of collapse. We describe here the methods for controlling the meniscus movement and the nanostructure collapse, and the metrology used to analyze the collapsed structures.

4.2.1 Nanostructure fabrication

EBL was used to fabricate an array of linear nanostructures. HSQ was spin coated on a silicon substrate to a thickness of 120 nm. The thickness was determined by ellipsometry. A Raith 150 EBL system was used to expose line arrays with doses ranging from 18 nC/cm ($\sim 1.1 \times 10^4$ electrons/nm) to 28 nC/cm ($\sim 1.7 \times 10^4$ electrons/nm) at 30 kV acceleration voltage and 200 pA beam current. After exposure, the samples were developed in a high-contrast salty developer (1% NaOH and 4% NaCl in de-ionized water)[11] at 24°C for 4 min followed by a de-ionized water rinse for 3 min.

4.2.2 Spin drying process

To control the meniscus movement direction and the collapsing order of the nanostructures, we developed a spin drying process. After the samples were developed in a high-contrast salty developer and rinsed with de-ionized water, the samples were mounted on a spin dryer. To prevent undesired pattern collapse,

care was taken during the mounting step so that the patterned surface was always covered with de-ionized water. A couple drops of de-ionized water were added to the mounted sample to cover the whole surface. The samples were sequentially spin dried at 500 rpm for 15 s to create a thin water layer, 350 rpm for 105 s to control the meniscus movement and collapse the nanostructures, and 2000 rpm for 10 s to remove remaining water from the surface.

4.2.3 Metrology

Metrology was performed by examining the collapsed nanostructures using a scanning electron microscope (SEM) after spin drying. Top down SEM images were taken using a Raith 150 scanning electron microscope operated with 10 kV acceleration voltage and 6 mm working distance.

4.3 Results

We were able to control the collapse of line structures by controlling the meniscus movement using the spin drying process. We observed pairwise collapse of line structures and used this phenomenon to demonstrate information propagation and build a logic gate. Here, we describe and explain these results.

4.3.1 Paired collapse of nanostructures

Figure 4-1 shows linear nanostructures collapsed in pairs. In figure 4-1(b), the line structures were 70 nm long and 10 nm wide. The smaller pitch was 70 nm and the

larger pitch was 490 nm. The line structures could only collapse in one of the two directions: up or down. Due to the asymmetric capillary force introduced by the asymmetric geometry, the line structures always collapsed in pairs after spin drying. Therefore, we were able to control the collapsing direction by changing the pitch of the line arrays.

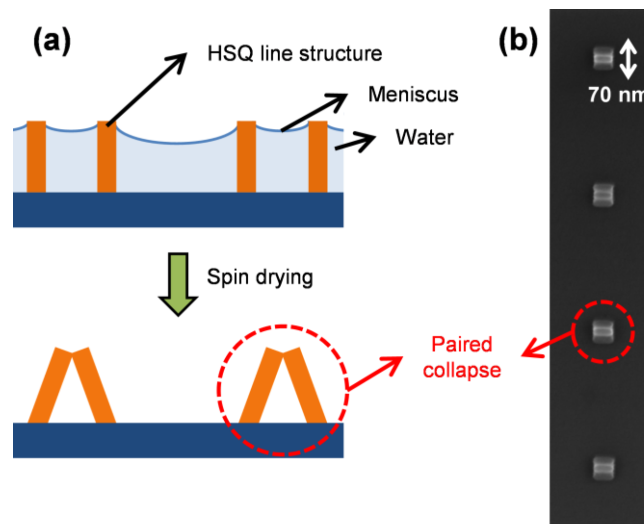

Figure 4-1: Paired collapse of line structures. (a) Schematic diagram showing the paired collapse. Asymmetric menisci caused the line structures to collapse toward each other. (b) SEM image of the line structures with two different pitches. The structures were collapsed in pairs after spin drying.

4.3.2 Propagation of information

Using the paired collapse of line structures, we demonstrated propagation of information as shown in figure 4-2. We developed two designs for achieving propagation of information. In figure 4-2(b), the line structures were 70 nm long and 10 nm wide. The pitch was 70 nm and the line structures were parallel to each

other. In figure 4-2(c), the line structures were 100 nm long and 10 nm wide. The pitch was 70 nm and the line structures were rotated by 45° from the parallel orientation so that the two neighboring walls were at a 90° angle. Even though the line arrays in both designs had a single pitch, we were still able to introduce asymmetric capillary force by controlling the direction of the meniscus movement via the spin drying process. If the meniscus moved from top to bottom, the first line structure would collapse towards the second line structure and form a pair. This step would be repeated as the meniscus moves downwards until all possible pairs are formed. Because the line structures always collapsed in pairs from the start, we were able to control the pairing of the final line structure by changing the number of structures in the line array. Even number (2N) of structures resulted in N pairwise collapsed structures whereas odd number (2N+1) of walls resulted in N pairwise collapsed structures and one unpaired structure. Therefore, we were able to propagate information about the parity of the line structures through the line array. This phenomenon could be used to perform computation.

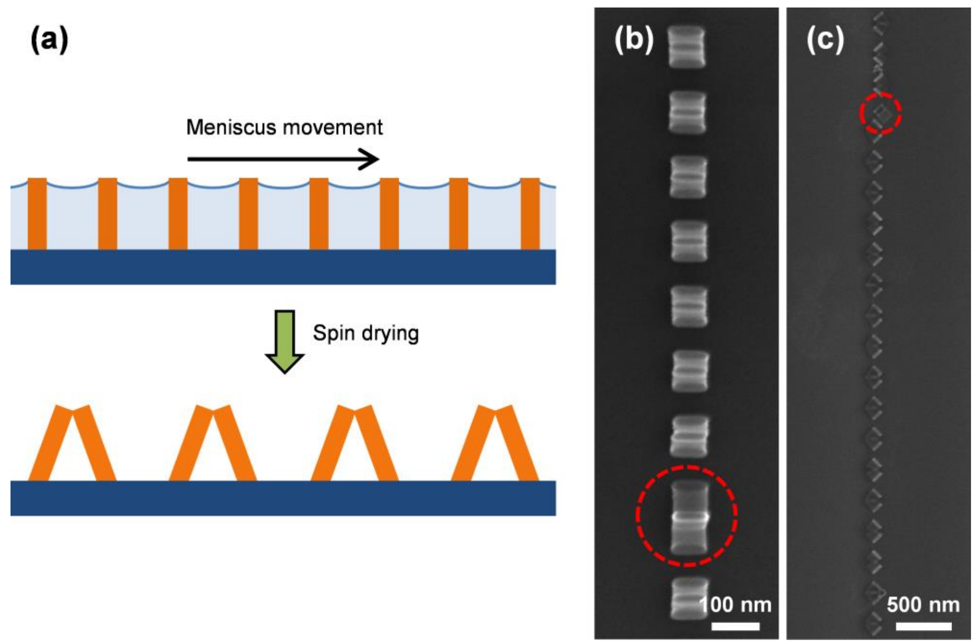

Figure 4-2: Propagation of information. (a) Schematic diagram showing the propagation of information. Asymmetric capillary force was created in symmetric geometry by controlling the direction of the meniscus movement. (b) SEM image of parallel line structures collapsed in pairs after spin drying. A defect (circled in red) was caused by three line structures collapsed together. (c) SEM image of line structures rotated by 45° collapsed in pairs after spin drying. A defect (circled in red) was caused by an unpaired line structure.

4.3.3 Collapse computation

Next, we designed a logic gate based on the parallel line structures. We used odd number of line structures as 1 bit and even number of line structures as 0 bit. Figure 4-3 shows our OR gate design where the OR gate is indicated by a red hexagon. As the meniscus moves from top to bottom, the line structures would collapse pairwise starting from the top as indicated by the arrows. When all three line structures inside the hexagon are standing when the meniscus moves through the hexagon, the three line structures would collapse toward the center as shown

in figure 4-3(a). However, in figure 4-3(b), the top left line structure inside the hexagon is already paired with a previous line structure when the meniscus reaches the hexagon. As a result, only two line structures remain standing inside the hexagon. The capillary force between the two line structures would be insufficient for pairwise collapse to occur and the line structures would be paired as shown in figure 4-3(b). In figure 4-3(c), the top two line structures inside the hexagon are already paired with neighboring line structures when the meniscus reaches the hexagon. Therefore, the remaining line structure would be paired as shown in figure 4-3(c). Figure 4-4 shows the collapsed line structures in an OR gate designed according to figure 4-3.

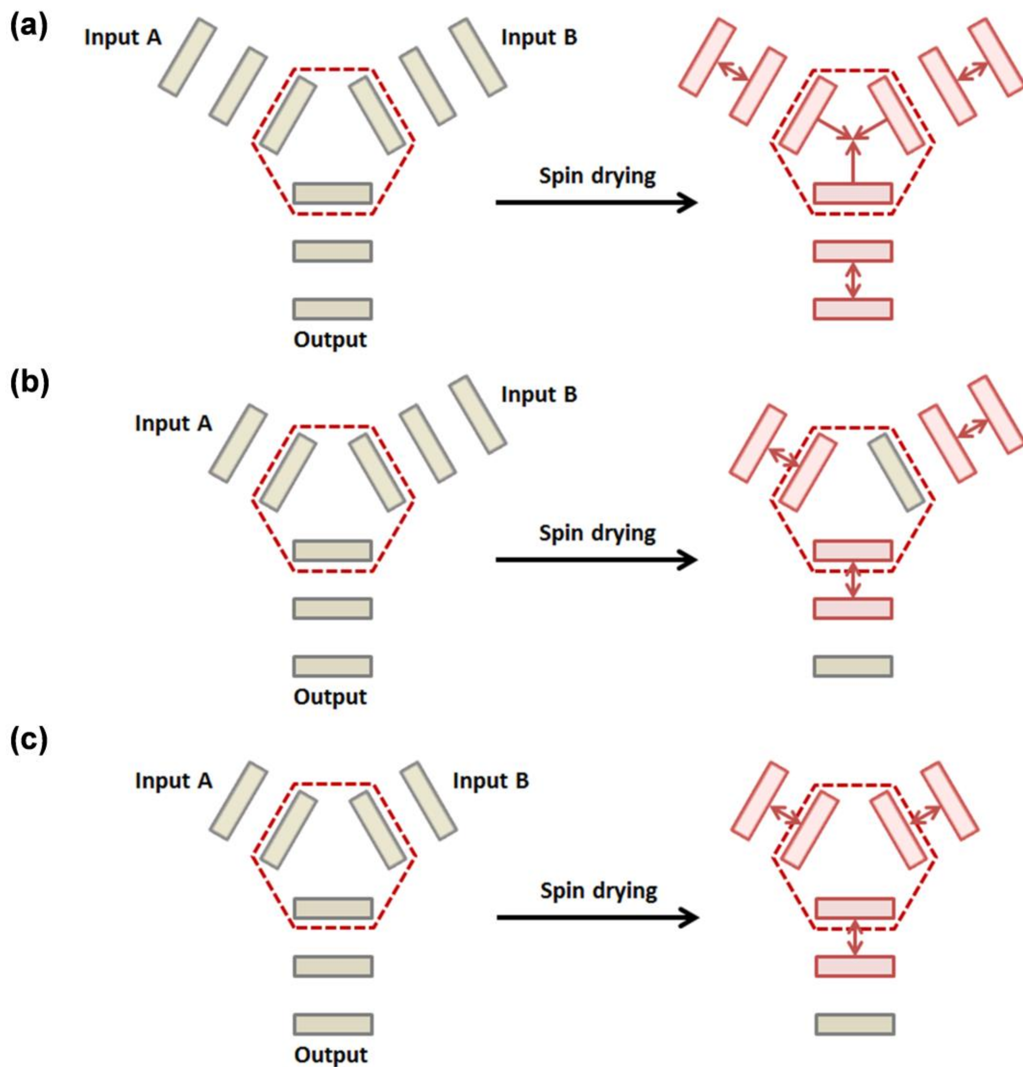

Figure 4-3: Schematic diagram showing OR gate design. OR gate is indicated by a red hexagon. Line structures before (left) and after (right) spin drying are shown. The arrows indicate the pairing of the collapsed line structures as the meniscus moves from top to bottom. (a) Both inputs had two line structures (0 bit). The output had no unpaired line structures after collapse (0 bit). (b) Input A had one line structure (1 bit) while input B had two line structures (0 bit). The output had one unpaired line structure after collapse (1 bit). (c) Both inputs had one line structure (1 bit). The output had one unpaired line structure after collapse (1 bit). Therefore, this is an OR gate.

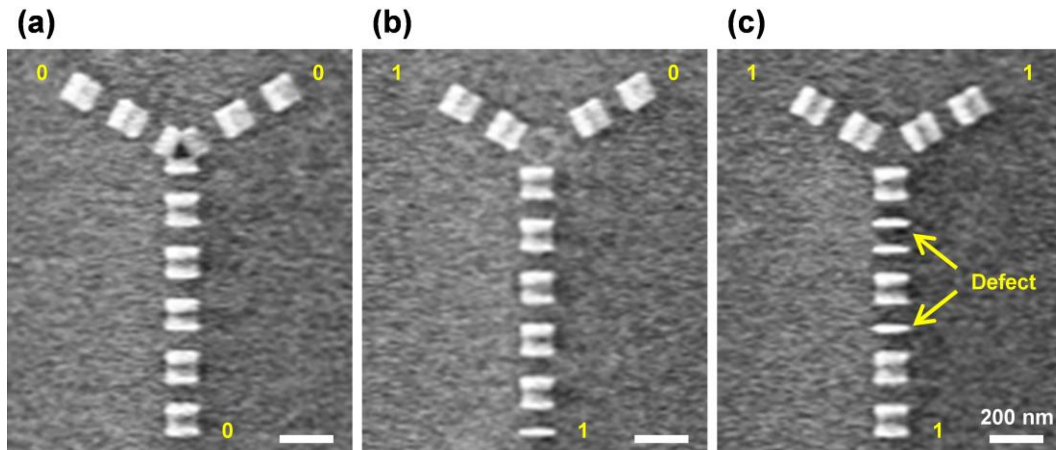

Figure 4-4: SEM images of collapsed line structures in an OR gate. (a) Both inputs had four line structures (0 bit). The output had no unpaired line structures after collapse (0 bit). (b) The left input had three line structures (1 bit) while the right input had four line structures (0 bit). The output had one unpaired line structure after collapse (1 bit). (c) Both inputs had three line structures (1 bit). The output had three unpaired line structures after collapse (1 bit). The first two standing line structures should have been paired with each other. The third standing line structure should have been paired with the next line structure so that the unpaired line structure appears at the end of the output instead of the middle.

4.4 Discussion

Different types of defects were observed in the collapsed line structures depending on the design. Moreover, parallel line structures were preferred over rotated line structures for its symmetric geometry. However, our logic gates showed low yield and high defect rate. We discuss the causes and solutions to these observations here.

Asymmetric geometry shown in figure 4-1 resulted in a defect-free paired collapse. However, several types of defects were found in symmetric geometry shown in figure 4-2. In parallel line structures, defects were caused by multiple

line structures collapsed together as in figure 4-2(b). When the line structures were exposed with lower dose, defects with more than three collapsed line structures were observed because the line width was decreased and the structures were easier to collapse. In rotated line structures, defects were caused by unpaired line structures as in figure 4-2(c). For both designs, some line structures remained standing even after spin drying when they were exposed with higher dose because the line width was increased.

Between the two designs used for the propagation of information, we chose the parallel line structures over the rotated line structures. Both designs showed good long-range order. For the rotated line structures, we experienced difficulties in merging two input line arrays into a single output line array due to the asymmetry of the design. When two arrays of rotated line structures were positioned close to each other, liquid meniscus was also formed between the two arrays. Therefore, line structure in one array was paired with the adjacent line structure in the other array. This prevented correct propagation of information. For the parallel line structures, we could build a logic gate as shown in figures 4-3 and 4-4. Still, the logic gates suffered from low yield and high defect rate. By optimizing the size and pitch of the line structures, we will develop and demonstrate a logic gate with a high yield.

4.5 Conclusions

We successfully demonstrated pairwise collapse of linear nanostructures. We achieved propagation of information and showed a proof of concept logic gate. By optimizing the various parameters of the line array, we hope to improve our logic gate in the future. With sufficiently high yield, we could eventually build a universal NOR gate or NAND gate to implement a simple circuit such as a half-adder. Our method for controlling the meniscus movement and the nanostructure collapse could possibly be used to fabricate self-assembled ordered complex patterns.

References

1. T. Tanaka, M. Morigami, and N. Atoda, Jpn. J. Appl. Phys., Part 1 **32,** 6059 (1993).
2. D. L. Goldfarb, J. J. de Pablo, P. F. Nealey, J. P. Simons, W. M. Moreau, and M. Angelopoulos, J. Vac. Sci. Technol. B **18,** 3313 (2000).
3. B. Pokroy, S. H. Kang, L. Mahadevan, and J. Aizenberg, Science **323,** 237 (2009).
4. D. Wu, Q.-D. Chen, B.-B. Xu, J. Jiao, Y. Xu, H. Xia, and H.-B. Sun, Appl. Phys. Lett. **95,** 091902 (2009).
5. M. De Volder, S. H. Tawfick, S. J. Park, D. Copic, Z. Zhao, W. Lu, and A. J. Hart, Adv. Mater. **22,** 4384 (2010).
6. S. H. Kang, B. Pokroy, L. Mahadevan, and J. Aizenberg, Nano Lett. **4,** 6323 (2010).
7. H. Duan and K. K. Berggren, Nano Lett. **10,** 3710 (2010).
8. M. P. Stoykovich, H. B. Cao, K. Yoshimoto, L. E. Ocola, and P. F. Nealey, Adv. Mater. **15,** 1180 (2003).
9. S. Choi, M. Yan, and I. Adesida, Appl. Phys. Lett. **93,** 163113 (2008).
10. H. Duan, J. K. W. Yang, and K. K. Berggren, Small **7,** 2661 (2011).
11. J. K. W. Yang and K. K. Berggren, J. Vac. Sci. Technol. B **25,** 2025 (2007).
12. J. K. W. Yang, B. M. Cord, H. Duan, J. Klingfus, S.-W. Nam, K.-B. Kim, M. J. Rooks, and K. K. Berggren, J. Vac. Sci. Technol. B **27,** 2622 (2009).

Chapter 5

Summary and future direction

We have investigated three major topics in this thesis: (1) three-dimensional (3D) nanofabrication using electron-beam lithography (EBL); (2) 3D nanofabrication using block copolymer (BCP) self-assembly; and (3) collapse computation using capillary force-induced self-assembly. Here, we summarize our work and provide ideas for future direction.

Chapter 2 shows two self-aligned methods of fabricating 3D nanostructures using EBL of hydrogen silsesquioxane (HSQ) and poly(methylmethacrylate) (PMMA) bilayer resist stack. The 3D nanostructures were used to guide the self-assembly of polystyrene-*b*-polydimethylsiloxane (PS-*b*-PDMS) BCP in Chapter 3. We expect that 3D nanostructures can be also fabricated using a multilayer resist stack with different resist combinations. We were able to fabricate freestanding structures using a bilayer resist stack with HSQ on top of PMMA. If we are able to fabricate 3D nanostructures with PMMA on top of HSQ, we could create

templates with two different structure heights. BCP self-assembly using these templates will lead to interesting results.

Chapter 3 shows a method of templating 3D nanostructures in PS-*b*-PDMS BCP thin films by using chemically functionalized 3D nanostructures as topographical templates. Although we observed 3D PDMS patterns, we were unable to form the PDMS patterns under the freestanding bridges. To fully utilize the 3D templates, the PDMS patterns must be formed under the freestanding structures so that the bottom layer as well as the top layer of the 3D template can direct the BCP self-assembly. To achieve this, we will use thermal annealing with lower molecular weight PS-*b*-PDMS (16 kg/mol, f_{PDMS} = 33%). Nanostructures other than mushroom-shaped posts and freestanding supported cross grids could also be used as 3D templates.

Chapter 4 shows a method of controlling the direction of the meniscus movement to guide the capillary force-induced self-assembly of linear nanostructures into complex 3D patterns. We developed a computation schema based on the pairwise collapse of nanostructures. We have not studied nanostructure arrangements other than parallel and rotated line arrays. However, different arrangements could be studied to create more complex 3D patterns. Our logic gates showed low yield and high defect rate because the parameters of the line array have not yet been optimized. If we can achieve higher yield after parameter optimization, multiple

logic gates could be combined to build a simple proof of concept circuit that can perform binary addition.